


Voltage-Controlled Ferromagnetic Resonance of Dipole-Coupled $\text{Co}_{40}\text{Fe}_{40}\text{B}_{20}$ Nanoellipses

Andres C. Chavez,¹ Joseph D. Schneider^{1,*}, Anthony Barra,¹ Sidhant Tiwari,² Robert N. Candler,^{2,3} and Gregory P. Carman¹

¹*Department of Mechanical and Aerospace Engineering, University of California, Los Angeles, California 90095, USA*

²*Department of Electrical and Computer Engineering, University of California, Los Angeles, California 90095, USA*

³*California NanoSystems Institute, Los Angeles, California 90095, USA*

 (Received 6 July 2019; revised manuscript received 6 September 2019; published 30 October 2019)

Multiuse or reconfigurable rf front ends require rf filters capable of dynamically broadening and/or shifting their operating frequency. Utilizing frequency-agile filters, the burden of signal processing is shifted from application specific hardware (e.g., application specific integrated circuit) to software-based solutions such as software defined radio (SDR). Current filter tuning approaches electrically modify surface or bulk acoustic wave signal absorption, but typically require prohibitively large electric fields to achieve large tuning. Alternatively, multiferroic based approaches overcome this limitation by leveraging magnetoelasticity to tune the ferromagnetic resonance (FMR) of nanostructures. Four configurations of $\text{Co}_{40}\text{Fe}_{40}\text{B}_{20}$ nanoellipses are simulated to theoretically demonstrate how voltage-induced strain and dipole-coupling affect their FMR spectra. For a single ellipse, two FMR peaks are observed, signifying primary (bulk) and secondary (edge) modes that were shifted up to approximately 2 GHz by a voltage-induced strain. For dipole-coupled ellipses, a third resonance peak develops in addition to the bulk and edge modes and similar frequency shifting is observed with equal strain applied to both nanostructures. When strain is applied to only one ellipse, fourth and fifth resonance peaks develop. The results demonstrate the high tunability of magnetoelastic based designs for future strain-based filtering, antennas, or computing applications.

DOI: [10.1103/PhysRevApplied.12.044071](https://doi.org/10.1103/PhysRevApplied.12.044071)

I. INTRODUCTION

Tunable rf filters, with the ability to broaden and shift operation frequency, are an essential component for flexible rf front ends [1,2]. Such frequency-agile filters provide the capability for reprogrammable devices that shift signal processing from application specific hardware (e.g., application specific integrated circuit) to software-based solutions such as software defined radio (SDR) [3,4]. Current rf filters are primarily surface acoustic wave (SAW) and bulk acoustic wave (BAW) devices due to their high quality factor (Q) and linear response [5,6]. Consequently, due to the electromechanical nature of these filters, most of the proposals for filter tuning involve materials with electric field-dependent elastic properties (i.e., stiffness) [3,4]. However, the voltage required to generate a sufficient tuning electric field for an approximately 10-MHz shift of the passband is often quite large [7]. One possible solution for larger tunability is to take advantage of the ferromagnetic

resonance [8] as a bandpass filter and use magnetoelasticity [9] as the tuning mechanism. Such a coupled approach can be achieved using multiferroic heterostructures.

The excitation and manipulation of magnetization using multiferroic materials has recently gained substantial interest due to their applications in memory [10–12], logic [13–16], nanobiotechnology [17–19], and rf (antenna) components [20–24]. Specifically, strain-powered multiferroics provide the promise of low power consumption. For example, nonvolatile magnetic memory storage can be realized by using strain to deterministically control the magnetization orientation in ferromagnetic nanoelements [12,25–27]. The potential to harness this energy efficiency in the context of rf electronics was also demonstrated by using strain generated from a piezoelectric substrate to manipulate the easy axis in a magnetostrictive material, causing spin waves to vary their propagation characteristics [28]. Similarly, dipole coupling in nanodot arrays has been manipulated via voltage-induced strain to create a binary logic wire, signifying the potential to directly modify electromagnetic coupling mechanisms. Dipole-coupled nickel disks have also been investigated

*jdschn02@g.ucla.edu

for their potential to produce artificial ferromagnet and antiferromagnet ordering in synthetic multiferroics [13]. Furthermore, dynamic manipulation of magnetization in a multiferroic has been shown to be useful for antenna applications due to elimination of the platform effect [20–22].

Leveraging the nonsymmetric properties of the permeability tensor, along with the field tunability of resonance properties of magnetic materials, numerous rf devices can be made with magnetic materials such as frequency modulators, Faraday-rotation isolators, phase shifters, and microwave power limiters, all of which require a magnetic bias field for operation and tunability [29,30]. Typically, ferrites are used for such devices, but these materials often lack the magnetostrictive properties that are often present in magnetoelastic materials. In this paper, a tunable filter is investigated that modifies the resonant and dipole modes of a nanodot array via magnetoelastic interactions in a multiferroic composite

II. MICROMAGNETIC SIMULATIONS

Our design for controlling FMR spectra consists of elliptical magnetoelastic $\text{Co}_{40}\text{Fe}_{40}\text{B}_{20}$ islands on a piezoelectric substrate as shown in Fig. 1(a). The ellipse material is chosen as $\text{Co}_{40}\text{Fe}_{40}\text{B}_{20}$ because of its large saturation magnetization and reasonable magnetostriction in comparison to other magnetoelastic materials such as Ni. Specifically, this is expected to offer larger tunability of the ferromagnetic resonance frequency due to increased dipole coupling and strain response. This design uses voltage-induced strains in the piezoelectric layer to introduce a magnetoelastic anisotropy that changes the resonance of the nanostructures. The magnetoelastic elements are numerically studied with a Landau-Lifshitz-Gilbert (LLG) micromagnetic formulation [31,32]

$$\frac{\partial \mathbf{m}}{\partial t} = -\mu_0 \gamma (\mathbf{m} \times \underline{H}_{\text{eff}}) + \alpha \left(\mathbf{m} \times \frac{\partial \mathbf{m}}{\partial t} \right), \quad (1)$$

where μ_0 is the permeability of free space, γ is the gyromagnetic ratio, and α is the Gilbert damping constant. The model neglects thermal fluctuations and assumes small elastic deformations as well as uniform strains within the magnetoelastic elements [16,33]. In Eq. (1), the effective magnetic field ($\underline{H}_{\text{eff}}$) for the system is the sum of the exchange field ($\underline{H}_{\text{ex}}$), demagnetization field (\underline{H}_d), and magnetoelastic field ($\underline{H}_{\text{me}}$). The magnetoelastic field is defined by $\underline{H}_{\text{me}} = 3\lambda_s Y(\varepsilon_x - \varepsilon_y)/\mu_0 M_s$, where λ_s is the saturation magnetostriction, Y is the Young's modulus, M_s is the saturation magnetization, and $(\varepsilon_x, \varepsilon_y)$ are the voltage-induced strains in the x and y directions, respectively. The biaxial strain difference can be produced experimentally by applying an electric field to patterned electrodes on the piezoelectric layer. The $\underline{H}_{\text{me}}$ term is represented in Eq. (1) by a uniform uniaxial anisotropy defined as

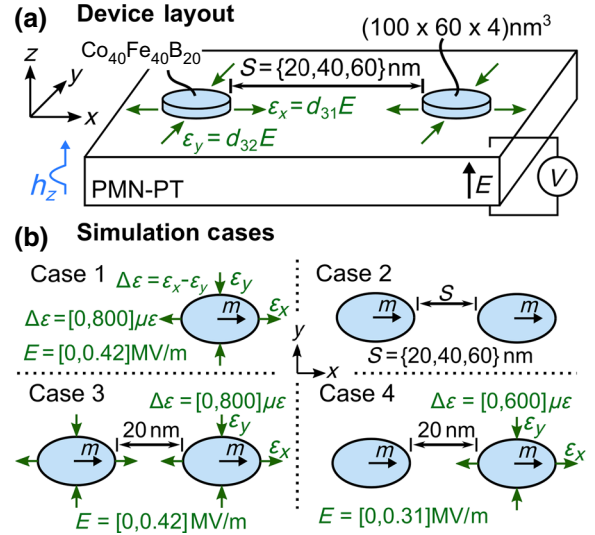


FIG. 1. Ellipse geometry for micromagnetic simulation. Applied Gaussian pulse magnetic field is directed through the thickness of the ellipse.

$K = \mu_0 M_s \underline{H}_{\text{me}}/2$ [16,34]. The LLG formulation is solved with the finite difference approach using a Dormand-Prince finite difference method [35,36].

To probe the FMR properties of the magnetoelastic ellipses, the magnetization is first allowed to reach an equilibrium state and then a magnetic Gaussian pulse (h_z) is applied through the element thickness (z axis). To reduce simulation time, the Gilbert damping constant is set to $\alpha_e = 0.3$ until an equilibrium state is reached. This typically takes approximately 2 ns of simulation time and once the equilibrium state is reached the Gilbert damping constant is returned to the actual material value. The process of starting the code with an artificially high α_e dramatically decreases the simulation time required to reach the equilibrium state without influencing the spin dynamics reorientation during the simulation [10,19]. For the dynamic regime, the damping parameter is then set to a more realistic value of $\alpha = 0.015$ [16] and the volume averaged magnetization $\mathbf{m}(t)$ of each nanostructure is recorded at uniform time intervals of 1 ps for another 4.1 ns of simulation time. The excitation field distribution in time is given by

$$h_z(t) = A \exp\left(\frac{4 \log(2)}{w^2}(t - b)^2\right), \quad (2)$$

where A is the peak height of the pulse, w is the full width at half maximum (FWHM) of the peak, b is the center of the peak, and t is time. This type of pulse is chosen because it is often used in experiments [37] and provides a significant broadband excitation of at least 20 GHz, which enables subsequent calculation of the magnetic susceptibility (χ) up to this frequency (i.e., in a range that is

suitable for typical device applications). The applied pulse is spatially uniform through the volume of the ellipses with a small amplitude of approximately 20 Oe chosen to minimize nonlinear behavior. Based on the choice of excitation field, the susceptibility in the frequency domain can be found from $M_z(\omega) = \mathbf{X}(\omega) \cdot \mathbf{H}(\omega)$ [38] by performing a Fast Fourier Transform (FFT) on the volume averaged $m_z(t)$. Here, the pulse parameters are: $A = 20$ Oe, $w = 10$ ps, and $b = 20$ ps.

In this paper, the FMR response of the magnetoelastic ellipse configurations shown in Fig. 1(b) are studied with an applied voltage-induced biaxial strain and, in a second case, when one ellipse is dipole-coupled to a single neighbor. The biaxial strain state ($\Delta\varepsilon$) is given by $\Delta\varepsilon = \varepsilon_x - \varepsilon_y$ and is chosen with a tensile strain (ε_x) directed along the x axis and a compressive strain (ε_y) directed along the y axis. This type of strain state is typical for strain-mediated multiferroics, and can be experimentally achieved by applying an electric field (E) through the thickness of a single crystal $[\text{Pb}(\text{Mg}_{1/3}\text{Nb}_{2/3})\text{O}_3]_{0.69}-[\text{PbTiO}_3]_{0.31}$ (PMN-PT) substrate, as shown in Fig. 1(b) [39]. In such cases, the corresponding strain values can be calculated from $\varepsilon_x = d_{31}E$ and $\varepsilon_y = d_{32}E$, where $d_{31} = 771$ pm/V and $d_{32} = -1147$ pm/V are the piezoelectric coefficients of the PMN-PT substrate [39]. Furthermore, finite element studies calculating the voltage-induced strain distribution in a PMN-PT substrate with closely patterned nanomagnets are conducted and indicate a highly localized strain is achievable. Specifically, patterned electrodes are used to localize the strain to a single ellipse with neighboring elements experiencing less than 6% of this strain. Hence, the use of a localized strain in the micromagnetic simulations of dipole-coupled ellipses is a reasonable approximation. Similar patterned electrodes have been utilized to generate localized strain in various magnetic nanostructures [12,27,33,40]. Using these voltage-induced biaxial strains, the FMR properties of the ellipses are studied in four cases, as shown in Fig. 1(b). Case 1 involves a single ellipse subjected to a biaxial strain that varies between 0 and $800 \mu\varepsilon$ in $200 \mu\varepsilon$ intervals corresponding to applied electric fields between 0 and 0.42 MV/m for 500-micron-thick PMN-PT. Case 2 focuses on two dipole-coupled ellipses, which are unstrained and have edge-to-edge separation distances of 20, 40, and 60 nm. Case 3 has two dipole-coupled ellipses with a separation distance of 20 nm subjected to equal biaxial strains equal to those in the first case. Finally, Case 4 involves two dipole-coupled ellipses separated by 20 nm, but with strain applied only to one of the ellipses, with strains ranging from 0 and $600 \mu\varepsilon$ in $200\text{-}\mu\varepsilon$ intervals, corresponding to applied electric fields between 0 and 0.31 MV/m.

The simulated ellipse geometry is $100 \times 60 \times 4$ nm³ for all cases. The dimensions and aspect ratio are chosen to ensure the ellipses are in a single domain state with shape anisotropy sufficient to keep the magnetization directed

TABLE I. Material properties for $\text{Co}_{40}\text{Fe}_{40}\text{B}_{20}$ nanoellipses.

| Material property | Symbol | Units | Value |
|--|-----------------|-------|-----------------------|
| Saturation magnetization | M_s | A/m | 1.2×10^6 |
| Gilbert damping (equilibrium state) | α_e | - | 0.3 |
| Gilbert damping (dynamic regime) | α | - | 0.015 |
| Exchange stiffness | A_{ex} | J/m | 1.9×10^{-11} |
| Saturation magnetostriction | λ_s | Ppm | 50 |
| Elastic modulus | Y | GPa | 160 |

in-plane along the major axis. This choice is made because such self-biasing would be advantageous in future device applications since it removes the requirement for an external magnetic bias field. Furthermore, with the material and geometries chosen for the simulation, all of the modeled nanodots would be thermally stable in experiment, with a shape anisotropy induced energy well of 70 K_bT (i.e., larger than the 40 K_bT required for modern magnetic random-access memories (MRAM) devices) [12]. All of the above-mentioned geometries are numerically simulated using a mesh with cubic elements (1 nm³) and with the material properties for $\text{Co}_{40}\text{Fe}_{40}\text{B}_{20}$, as given in Table I [16,41,42]. Furthermore, the mesh is verified by using the built-in function edgesmooth that produces results similar to the results without edgesmooth. This result indicates that the solution has converged to the actual solution dictated by a smooth geometry.

III. RESULTS AND DISCUSSION

Figures 2(a)–2(e) show the FMR response of a single $\text{Co}_{40}\text{Fe}_{40}\text{B}_{20}$ ellipse when a voltage-induced biaxial strain is applied. Figure 2(a) shows the susceptibility along the z axis of the $\text{Co}_{40}\text{Fe}_{40}\text{B}_{20}$ ellipse as a function of frequency for electric fields of 0 to 0.42 MV/m. As seen from the figure, the susceptibility exhibits two peaks, which are designated as bulk and edge modes. Specifically, the largest peak is the bulk mode and the secondary peak is the edge mode. As the strain is increased, both the bulk and edge modes shift up in frequency by similar amounts. For example, at 0.10 MV/m, the bulk mode frequency is 7.32 GHz and the edge mode frequency is 12.45 GHz. Increasing the electric field to 0.31 MV/m results in bulk and edge mode frequencies of 7.81 and 12.93 GHz, respectively. Figures 2(b)–2(e) show the dynamics of m_z for two bulk modes ($P1, P3$) and two edge modes ($P2, P4$) of the ellipse. These mode shapes are shown for the modes $P1 = 6.84$ GHz and $P2 = 12.21$ GHz when the system is unstrained, and for $P3 = 7.81$ GHz and $P4 = 12.93$ GHz when the system is strained by applying 0.31 MV/m to the PMN-PT substrate. The mode shapes shown are selected after reviewing the entire dynamic images of the spin excitations. The snapshots selected best convey the resonance values and are

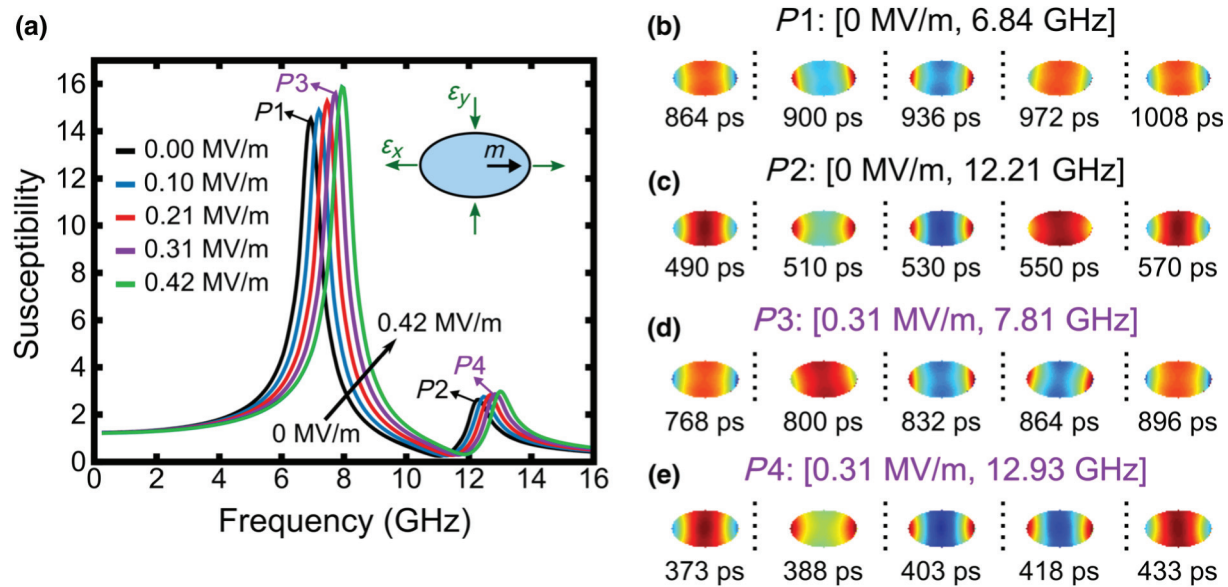


FIG. 2. (a) Susceptibility of $\text{Co}_{40}\text{Fe}_{40}\text{B}_{20}$ ellipse when subjected to voltage-induced biaxial strain. Magnetic excitation is generated by a Gaussian pulse magnetic field directed through the thickness of the ellipse. (b)–(e) Normalized mode shapes generated by simulation software for peaks $P1$ – $P4$.

obtained at approximately a quarter of a period. Specifically, this quarter-period time interval corresponds with the peaks of a sinusoidal magnetic driving field with the same frequency. So, for example, the magnetic state for the peak at 6.84 GHz is recorded at time intervals of 36 ps, while a 6.84 GHz low-amplitude driving field simultaneously excites this system. Each mode shape image is then color normalized by a maximum RGB value that corresponds to the maximum magnitude of m_z . Since the maximum value of m_z is different for each image, the normalization factor is also unique, meaning that the colors in each image cannot be directly compared. Instead, the mode shapes are intended only to show general trends regarding the location of standing wave nodes, as this is sufficient to show the strain-induced mode modulation that is the focus of this paper. From Fig. 2, it is clear that the mode shapes for $P1$ and $P3$ are similar and the mode shapes of $P2$ and $P4$ are also similar.

The large peak in the susceptibility is from the bulk magnetization, while the small peak is due to the demagnetization effect along the periphery of the ellipse. Since the small peak is due to the demagnetization effect, the position and shape of the small peak would change if the aspect ratio is changed. The voltage-induced changes in the single $\text{Co}_{40}\text{Fe}_{40}\text{B}_{20}$ ellipse's susceptibility values (Fig. 2) are explained using the magnetoelastic response of the nanostructure. The applied electric field results in tensile and compressive strains directed along the major and minor axes of the ellipse, respectively. Since $\text{Co}_{40}\text{Fe}_{40}\text{B}_{20}$ is a positive magnetoelastic material, the applied strains cause the magnetization to favor orientation along the

major axis of the ellipse. This effectively makes the major axis magnetically stiffer resulting in a higher ferromagnetic resonance frequency observed as the peaks shift to the right with increasing electric field (i.e., strain). This is analogous to a mechanical spring-mass system in which the natural frequency increases with spring stiffness. This analogy can be further understood by considering the Kittel Equation

$$\omega = \gamma \mu_0 \sqrt{[(N_x - N_z)M_x - H_{\text{eff}}][(N_y - N_z)M_x - H_{\text{eff}}]}, \quad (3)$$

where ω is the ferromagnetic resonance frequency, the effective field (H_{eff}) is the effective field due to mechanical strain, and the N_i are the demagnetization factors along the x , y , and z axes, respectively. For the geometry used in this paper, $N_x \approx 0.046$, $N_y \approx 0.078$, and $N_z \approx 0.875$. Comparison between simulation and calculation of FMR using the above relation, shows a strong agreement. For example, at an applied electric field of 0.42 MV/m, the simulation predicts a resonance of 8.03 GHz while the calculation results in 8.05 GHz. Similar agreement is found for the other applied electric fields with 1.4% being the largest error between simulation and experiment for an applied electric field of 0.21 MV/m.

Figures 3(a)–3(d) show the FMR response changes of two dipole-coupled $\text{Co}_{40}\text{Fe}_{40}\text{B}_{20}$ ellipses as their separation distance (S) increases from 20 to 60 nm. Figure 3(a) shows the susceptibility of the dipole-coupled ellipses as a function of frequency. In this case, the susceptibility is determined by taking the FFT of the volume-averaged magnetic z component $m_z(t)$ of the dipole-coupled system.

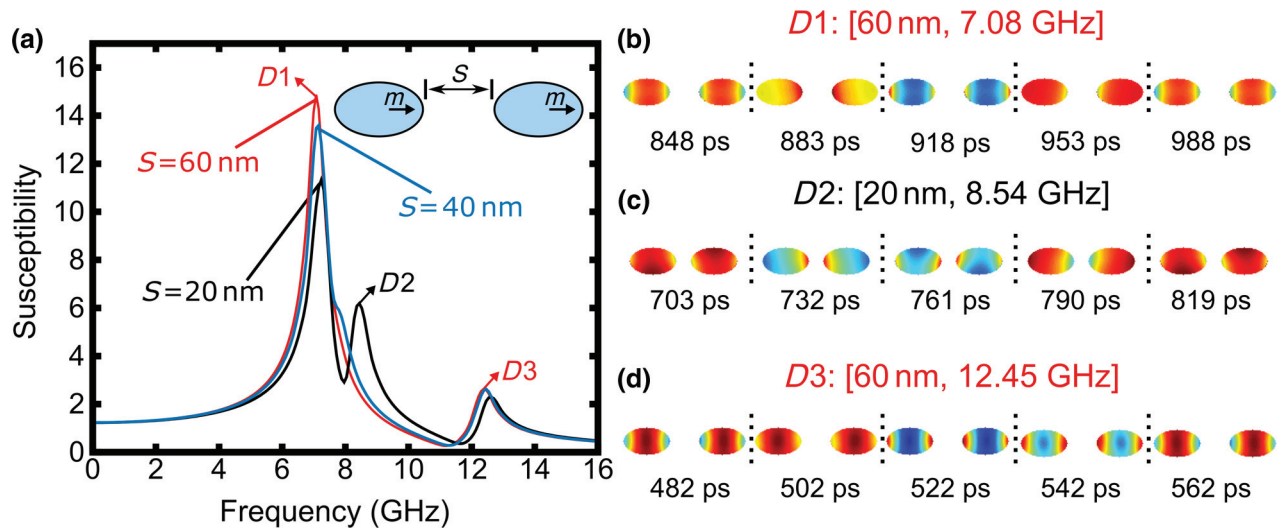


FIG. 3. (a) Susceptibility of two dipole-coupled $\text{Co}_{40}\text{Fe}_{40}\text{B}_{20}$ ellipses for separation distances $S = \{20, 40, 60\}$ nm. (b)–(d) Normalized mode shapes generated by simulation software for peaks $D1$ – $D3$.

In contrast to the single ellipse case, Fig 3(a) shows that at 20-nm separation, the dipole-coupled system exhibits three resonance peaks. Inspection of the plot shows that the largest and smallest peaks resemble the bulk and edge modes in the single ellipse case, while the peak labeled $D2$ is new. When the separation is increased to 40 nm, it is seen that the new $D2$ peak is reduced to a small bump near 7.9 GHz and ultimately disappears once the separation distance is 60 nm. Figures 3(b)–3(d) show the mode shapes of the dipole-coupled system at frequencies $D1 = 7.08$ GHz, $D2 = 8.54$ GHz, and $D3 = 12.45$ GHz for 60-, 20-, and 60-nm separation distances, respectively. The mode shapes are obtained using the same method as in the single ellipse case. The mode shapes for peaks $D1$ and $D3$ resemble the bulk and edge mode shapes for the single ellipse case, respectively. The mode shape for $D2$ does not resemble any of the single ellipse mode shapes and exhibits an antialigned shape. The observed splitting of the dipole mode is similar to the mode splitting seen in other coupled resonators used in rf filters, such as MEMS, electromagnetic, and surface acoustic wave resonators [43–48]. This is shown by the alternating regions of dark and light colors within the central regions of the ellipses in Fig. 3(c).

The effects of separation distance on the FMR spectra of two dipole-coupled ellipses are explained by the strength of the dipole coupling between the two magnetoelastic elements. In particular, as the separation distance increases, the dipole coupling necessarily decreases nonlinearly. Given this inherent decrease in coupling strength with separation distance, it follows that past some critical distance, there is effectively no dipole coupling between the ellipses. Past this critical distance, there would effectively be two isolated magnetoelastic elements and an FMR response similar to the single ellipse case would be

expected. Thus, the peak labeled $D2$ is no longer present, resulting in an increased susceptibility at the primary frequency. This trend is exactly what the simulations show because the third peak ($D2$) is present for the 20-nm separation distance and gradually disappears until the separation reaches 60 nm where the FMR spectra has only two peaks centered almost exactly at the frequencies of the single ellipse case.

Figure 4 shows the FMR response changes of two dipole-coupled elements separated by 20 nm when a voltage-induced biaxial strain is applied to both ellipses. The two ellipses are subjected to the same applied electric field (i.e., same strain state) and the electric field is varied from 0.00 to 0.42 MV/m. The susceptibility exhibits three peaks and, as the electric field is increased, each peak shifts

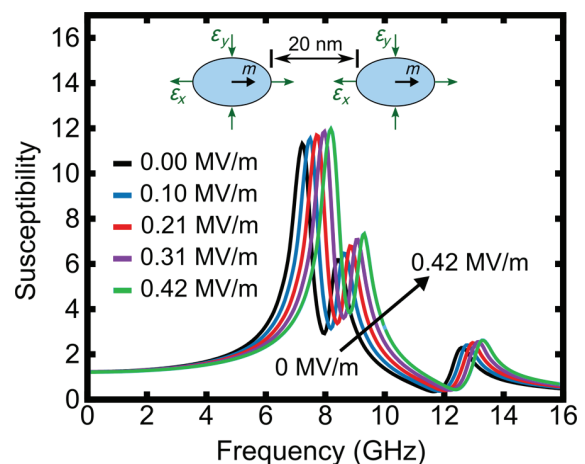


FIG. 4. Ellipse geometry for micromagnetic simulation. An applied Gaussian pulse magnetic field is directed through the thickness of the ellipse.

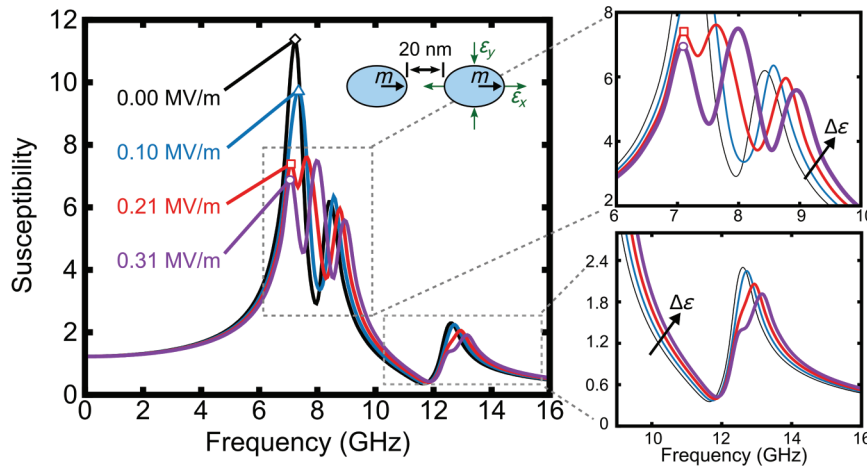


FIG. 5. Ellipse geometry for micromagnetic simulation. An applied Gaussian pulse magnetic field is directed through the thickness of the ellipse.

up in frequency equally. For example, when the electric field is increased from 0.10 to 0.31 MV/m, the three resonance peaks increase from {7.56, 8.54, 12.69} GHz to {8.05, 9.03, 13.18} GHz. Finally, the largest, middle, and smallest peaks correspond to the bulk, dipole, and edge modes.

The FMR changes for the dipole-coupled ellipses separated by 20 nm (Fig. 4) and subjected to equal voltage-induced biaxial strains are caused by the previously discussed strain and dipole effects. Specifically, the appearance of a third (middle) peak for these FMR responses is a consequence of the strong dipole coupling at 20 nm seen in the previous simulations. Furthermore, the shift of the resonance curves with increased electric field is explained by the Kittel equation for the single ellipse case. It is interesting to note that the combined effect of strain and dipole coupling appear as a superposition of the two effects. This is reasonable since the model assumptions imply the studied system is linear in terms of mechanics (i.e., linear magnetoelasticity) and also follows linear magnetization dynamics (i.e., due to the small angle of magnetization precession).

Figure 5 shows the FMR response changes of two dipole-coupled ellipses that vary when a voltage-induced biaxial strain is applied to only one of the structures. In this case, the separation distance is chosen as 20 nm and the electric field is varied from 0.00 to 0.31 MV/m. For a zero-applied electric field, the susceptibility exhibits only three resonance peaks and the bulk mode is identified by the diamond-shaped marker on the plot. Similarly, only three resonance peaks occur for 0.10 MV/m and the bulk mode is identified by the triangular marker. At 0.21 MV/m, four resonance peaks are seen and a square marker is used to identify the bulk mode at this electric field. Inspection of the inset shows that the first three resonance peaks occur at 7.08, 7.56, and 8.78 GHz, while the edge mode peak occurs at 12.93 GHz. At 0.31 MV/m, a fifth resonance peak appears near the edge mode. The five resonances for this case occur at 7.08, 8.05, 9.03, 12.45, and 13.83 GHz.

As in the previous simulation case, a combined effect of mechanics and dipole coupling explains the changes in FMR spectra for the two-magnet system with voltage-induced biaxial strain applied to only one element (Fig. 5). Without an applied electric field, the expected three-peak spectra are obtained since only dipole coupling is present. When the electric field is increased to 0.10 MV/m, three peaks are still present, but there is a slight shift consistent with the increasing field. The first (bulk) mode is centered at 7.3 GHz, which is the same value as the single ellipse case at that applied field. Notably, the first peak is slightly broadened in comparison to the zero-applied electric field case. This results from the superposition of the mechanical and dipole effects previously discussed. Specifically, in the previous simulation case, the bulk mode frequency for the unstrained dipole system is 7.08 GHz. Due to superposition, this peak is not lost in the case of Fig. 5, but instead combines with the 7.3 GHz peak resulting in the broadened bulk mode of the 0.10 MV/m response. As the electric field is increased to 0.21 MV/m, a separation between these two peaks is seen. Specifically, there is still a 7.08-GHz peak corresponding to the unstrained dipole bulk mode while the second peak is further shifted to 7.56 GHz (matching the corresponding single ellipse case at 0.21 MV/m). Consequently, the appearance of a fourth peak is a result of causing a large enough distinction between the FMR responses of the individual strained and unstrained ellipses. Similarly, this superposition of the individual FMR peaks of each ellipse explains the response at 0.31 MV/m. The additional consequence is that there is now sufficient separation between the edge mode peaks of the strained and unstrained ellipses such that a fifth distinct peak appears. Based on these results, it is reasonable to speculate that increasing the number of dipole-coupled elements and trying different strain combinations would increase the number of peaks and increase the tunability of FMR, thus opening the possibility for alternative strain-based filtering, antennas, or computing devices that rely on rf operating principles.

IV. CONCLUSION

The results demonstrate the large tunability of ferromagnetic resonance spectra with applied voltage-induced strain. Specifically, the resonance peaks are shown to be deterministically shifted with applied strain. Furthermore, combining the effects of strain with dipole coupling leads to significant modulation of the FMR spectra. For example, simulation indicated the combination of dipole coupling with strain not only shifts resonance peaks, but also introduces new ones in the two-magnet systems. Finally, the results open avenues for further investigation regarding increasing the number of coupled elements and varying combinations of strain for future strain-based filtering, antennas, or computing device applications such as software defined radio.

ACKNOWLEDGMENTS

This work was supported by NSF Nanosystems Engineering Research Center for Translational Applications of Nanoscale Multiferroic Systems (TANMS) Cooperative Agreement Grant No. EEC-1160504 and EFRI NewLaw with Grant No. 1641128.

-
- [1] K. Y. Hashimoto, S. Tanaka, and M. Esashi, in 2011 Joint Conference of the IEEE International Frequency Control and the European Frequency and Time Forum (FCS) Proceedings (2011).
- [2] J. F. Luy, T. Mueller, T. Mack, and A. Terzis, Configurable RF receiver architectures, *IEEE Microw. Mag.* **5**, 75 (2004).
- [3] R. Aigner, Tunable filters? Reality check foreseeable trends in system architecture for tunable RF filters, *IEEE Microw. Mag.* **16**, 82 (2015).
- [4] S. Gevorgian, A. Tagantsev, and A. K. Vorobiev, *Tunable Film Bulk Acoustic Wave Resonators* (Springer-Verlag, London, 2013).
- [5] C. Campbell, *Surface Acoustic Wave Devices and Their Signal Processing Applications* (Academic Press, INC, San Diego, 1989).
- [6] K. Hashimoto, editor, *RF Bulk Acoustic Wave Filters for Communications* (Artech House, Norwood, 2009).
- [7] A. Noeth, P. Muralt, A. K. Tagantsev, N. Setter, and T. Yamada, Tunable thin film bulk acoustic wave resonator based on $\text{Ba}_x\text{Si}_{1-x}\text{TiO}_3$ thin film, *IEEE Trans. Ultrason. Ferroelectr. Freq. Control* **57**, 379 (2010).
- [8] C. Kittel, On the theory of ferromagnetic resonance absorption, *Phys. Rev.* **73**, 155 (1948).
- [9] S. Chikazumi, *Physics of Ferromagnetism* (Oxford University Press, Oxford, 1997).
- [10] C.-Y. Y. Liang, S. M. Keller, A. E. Sepulveda, A. Bur, W.-Y. Y. Sun, K. Wetzlar, and G. P. Carman, Modeling of magnetoelastic nanostructures with a fully coupled mechanical-micromagnetic model, *Nanotechnology* **25**, 435701 (2014).
- [11] X. Li, D. Carka, C. Liang, A. E. Sepulveda, S. M. Keller, P. K. Amiri, G. P. Carman, and C. S. Lynch, Strain-mediated 180° perpendicular magnetization switching of a single domain multiferroic structure, *J. Appl. Phys.* **118**, 14101 (2015).
- [12] Q. Wang, X. Li, C.-Y. Y. Liang, A. Barra, J. Domann, C. Lynch, A. Sepulveda, and G. Carman, Strain-mediated 180° switching in CoFeB and Terfenol-D nanodots with perpendicular magnetic anisotropy, *Appl. Phys. Lett.* **110**, 102903 (2017).
- [13] A. C. Chavez, W. Y. Sun, J. Atulasimha, K. L. Wang, and G. P. Carman, Voltage induced artificial ferromagnetic-antiferromagnetic ordering in synthetic multiferroics, *J. Appl. Phys.* **122**, 224102 (2017).
- [14] A. C. Chavez, A. Barra, and G. P. Carman, Voltage control of magnetic monopoles in artificial spin ice, *J. Phys. D: Appl. Phys.* **51**, 234001 (2018).
- [15] R. Lo Conte, Z. Xiao, C. Chen, C. V. Stan, J. Gorchon, A. El-Ghazaly, M. E. Nowakowski, H. Sohn, A. Pattabi, A. Scholl, N. Tamura, A. Sepulveda, G. P. Carman, R. N. Candler, and J. Bokor, Influence of nonuniform micron-scale strain distributions on the electrical reorientation of magnetic microstructures in a composite multiferroic heterostructure, *Nano Lett.* **18**, 1952 (2018).
- [16] I. Gilbert, A. C. Chavez, D. T. Pierce, J. Unguris, W.-Y. Y. Sun, C.-Y. Y. Liang, and G. P. Carman, Magnetic microscopy and simulation of strain-mediated control of magnetization in PMN-PT/Ni nanostructures, *Appl. Phys. Lett.* **109**, 162404 (2016).
- [17] Z. Xiao, K. P. Mohanchandra, R. Lo Conte, C. Ty Karaba, J. D. Schneider, A. Chavez, S. Tiwari, H. Sohn, M. E. Nowakowski, A. Scholl, S. H. Tolbert, J. Bokor, G. P. Carman, and R. N. Candler, Enhanced magnetoelectric coupling in a composite multiferroic system via interposing a thin film polymer, *AIP Adv.* **8**, 55907 (2018).
- [18] H. Sohn, M. E. Nowakowski, C. Liang, J. L. Hockel, K. Wetzlar, S. Keller, B. M. McLellan, M. A. Marcus, A. Doran, A. Young, M. Kläui, G. P. Carman, J. Bokor, and R. N. Candler, Electrically driven magnetic domain wall rotation in multiferroic heterostructures to manipulate suspended on-chip magnetic particles, *ACS Nano* **9**, 4814 (2015).
- [19] Z. Xiao, R. Lo Conte, C. Chen, C.-Y. Liang, A. Sepulveda, J. Bokor, G. P. Carman, and R. N. Candler, Bi-directional coupling in strain-mediated multiferroic heterostructures with magnetic domains and domain wall motion, *Sci. Rep.* **8**, 5207 (2018).
- [20] Z. Yao, Y. E. Wang, S. Keller, and G. P. Carman, Bulk acoustic wave-mediated multiferroic antennas: Architecture and performance bound, *IEEE Trans. Antennas Propag.* **63**, 3335 (2015).
- [21] J. P. Domann and G. P. Carman, Strain powered antennas, *J. Appl. Phys.* **121**, 44905 (2017).
- [22] T. Nan, et al., Acoustically actuated ultra-compact NEMS magnetoelectric antennas, *Nat. Commun.* **8**, 1 (2017).
- [23] P. Withers, Electromagnetic mirrors in the sky: Accessible applications of Maxwell's equations, *Am. J. Phys.* **83**, 506 (2015).
- [24] X. Yang, Y. Gao, J. Wu, Z. Zhou, S. Beguhn, T. Nan, and N. X. Sun, Voltage tunable multiferroic phase shifter with YIG/PMN-PT heterostructure, *IEEE Microw. Wirel. Compon. Lett.* **24**, 191 (2014).
- [25] A. A. Kundu, A. C. Chavez, S. M. Keller, G. P. Carman, and C. S. Lynch, 360° deterministic magnetization rotation

- in a three-ellipse magnetoelectric heterostructure, *J. Appl. Phys.* **123**, 104105 (2018).
- [26] C.-Y. Y. Liang, S. M. Keller, A. E. Sepulveda, W.-Y. Y. Sun, J. Cui, C. S. Lynch, and G. P. Carman, Electrical control of a single magnetoelastic domain structure on a clamped piezoelectric thin film—analysis, *J. Appl. Phys.* **116**, 123909 (2014).
- [27] A. Barra, J. Domann, K. W. Kim, and G. Carman, Voltage Control of Antiferromagnetic Phases at Near-Terahertz Frequencies, *Phys. Rev. Appl.* **9**, 34017 (2018).
- [28] M. Balinskiy, A. C. Chavez, A. Barra, H. Chiang, G. P. Carman, and A. Khitun, Magnetoelastic spin wave modulator based on synthetic multiferroic structure, *Sci. Rep.* **8**, 10867 (2018).
- [29] D. M. Pozar, *Microwave Engineering*, 4th ed. (John Wiley & Sons, Inc, Hoboken, 2012).
- [30] B. Lax and K. Button, *Microwave Ferrites and Ferromagnetics* (McGraw-Hill Book Company, Inc., New York, n.d.).
- [31] T. L. Gilbert, Classics in magnetism a phenomenological theory of damping in ferromagnetic materials, *IEEE Trans. Magn.* **40**, 3443 (2004).
- [32] M. Lakshmanan, The fascinating world of the Landau–Lifshitz–Gilbert equation: An overview, *Philos. Trans. R. Soc. A Math. Phys. Eng. Sci.* **369**, 1280 (2011).
- [33] J. Cui, C.-Y. Liang, E. A. Paisley, A. Sepulveda, J. F. Ihlefeld, G. P. Carman, and C. S. Lynch, Generation of localized strain in a thin film piezoelectric to control individual magnetoelectric heterostructures, *Appl. Phys. Lett.* **107**, 92903 (2015).
- [34] B. D. Cullity and C. Graham, *Introduction to Magnetic Materials*, 2nd ed. (Wiley, New York, 2009).
- [35] A. Vansteenkiste, J. Leliaert, M. Dvornik, M. Helsen, F. Garcia-Sanchez, and B. Van Waeyenberge, The design and verification of MuMax3, *AIP Adv.* **4**, 107133 (2014).
- [36] A. Vansteenkiste and B. Van de Wiele, MuMax: A new high-performance micromagnetic simulation tool, *J. Magn. Mater.* **323**, 2585 (2011).
- [37] B. B. Maranville, R. D. McMichael, S. A. Kim, W. L. Johnson, C. A. Ross, and J. Y. Cheng, Characterization of magnetic properties at edges by edge-mode dynamics, *J. Appl. Phys.* **99**, 97 (2006).
- [38] R. D. McMichael and M. D. Stiles, Magnetic normal modes of nanoelements, *J. Appl. Phys.* **97**, 10J901 (2005).
- [39] PMN-31PT Data Sheet (n.d.).
- [40] J. Cui, J. L. Hockel, P. K. Nordeen, D. M. Pisani, C. Y. Liang, G. P. Carman, and C. S. Lynch, A method to control magnetism in individual strain-mediated magnetoelectric islands, *Appl. Phys. Lett.* **103**, 232905 (2013).
- [41] C. Burrowes, N. Vernier, J.-P. Adam, L. Herrera Diez, K. Garcia, I. Barisic, G. Agnus, S. Eimer, J.-V. Kim, T. Devolder, A. Lamperti, R. Mantovan, B. Ockert, E. E. Fullerton, and D. Ravelosona, Low depinning fields in Ta-CoFeB-MgO ultrathin films with perpendicular magnetic anisotropy, *Appl. Phys. Lett.* **103**, 182401 (2013).
- [42] X. Liu, W. Zhang, M. J. Carter, and G. Xiao, Ferromagnetic resonance and damping properties of CoFeB thin films as free layers in MgO-based magnetic tunnel junctions, *J. Appl. Phys.* **110**, 33910 (2011).
- [43] S. A. Bhave, D. Gao, R. Maboudian, and R. T. Howe, in 18th IEEE International Conference on Micro Electro Mechanical Systems, 2005. MEMS 2005 (2005), pp. 223–226.
- [44] G. Endoh, M. Ueda, O. Kawachi, and Y. Fujiwara, High performance balanced type SAW filters in the range of 900 MHz and 1.9 GHz, *Proc. IEEE Ultrason. Symp.* **1**, 41 (1997).
- [45] J. Hong and M. J. Lancaster, Cross-coupled microstrip hairpin-resonator filters, **46**, 118 (1998).
- [46] T. Morita, Y. Watanabe, M. Tanaka, and Y. Nakazawa, Wideband low loss double mode SAW filters (2003), p. 95.
- [47] C. T. C. Nguyen, Frequency-selective MEMS for miniaturized low-power communication devices, *IEEE Trans. Microw. Theory Tech.* **47**, 1486 (1999).
- [48] P. Gay-Balmaz and O. J. F. Martin, Electromagnetic resonances in individual and coupled split-ring resonators, *J. Appl. Phys.* **92**, 2929 (2002).